Construction and Building Materials 328 (2022) 126899

Contents lists available at ScienceDirect

Construction and Building Materials

journal homepage: www.elsevier.com/locate/conbuildmat

An alternative approach for measuring the mechanical properties of hybrid concrete through image processing and machine learning

Muhammad Imran Waris [a], Vagelis Plevris [b,*], Junaid Mir [c], Nida Chairman [d], Afaq Ahmad [a]

[a] Department of Civil Engineering, University of Engineering and Technology, Taxila, Pakistan
[b] Department of Civil and Architectural Engineering, Qatar University, Qatar
[c] Department of Electrical Engineering, University of Engineering and Technology, Taxila, Pakistan
[d] School of Applied Management, University of Westminster, United Kingdom

ARTICLE INFO

Keywords:
Artificial neural network
Adaptive neuro-fuzzy inference system
Image processing
Hybrid concrete
Silica fume
Fly ash

ABSTRACT

Image processing (IP), artificial neural network (ANN), and adaptive neuro-fuzzy inference system (ANFIS) are innovative techniques in computer science that have been widely used to predict the properties of materials in structural engineering. The stability of reinforced concrete structures mainly depends on the mechanical properties of concrete, i.e., its compressive strength f_c and tensile strength f_t. Different kinds of inexpensive cement replacement materials (CRM) can be used to form hybrid concrete (HC) with enhanced mechanical and other properties. In this study, the IP, ANN, and ANFIS methods are properly combined and used to predict the mechanical properties of hybrid concrete. For this, 162 cylindrical specimens of HC with 0%, 15%, and 25% silica fume and fly ash as replacement material with three mix ratios, 1:3:6, 1:2:4, and 1:1.5:3 were cast at 14 days and 28 days curing. The specimens were divided into three equal sets as follows: (i) the first to find the compressive strength, (ii) the second to find the split cylinder strength, and (iii) the third to develop a database of images. For the image acquisition, each cylinder of the third set is cut into three slices using a stone cutting saw, resulting in six faces and a total of 324 images (6 × 54). Photos (digital images) are then taken in fully controlled lighting conditions from a height of 600 mm between the concrete surface and the camera lens. The acquired images are pre-processed (converted to grayscale, cropped, and resized to 256 × 256 pixels), and the statistical features are extracted to predict the f_c and f_t by using ANN and ANFIS techniques. Finally, the predicted values are tested and validated through nondestructive testing methods. The actual values of the compressive and the tensile strength of concrete were compared to the corresponding values estimated by the proposed methods, i.e. (IP, ANN) and (IP, ANFIS). The accuracy of the results largely depends on the data set. The accuracy obtained by IP/ANN is 99.7% while the one obtained with IP/ANFIS is 97.8%.

1. Introduction

Over the last decades, image processing (IP) and artificial neural networks (ANN) have been frequently applied to solve categorization and prediction problems in many scientific and engineering domains. In civil engineering, these methods have been applied as alternative problem-solving techniques for problems associated with structural health monitoring (SHM) [1], among various other applications. SHM is crucial for taking preventive measures for possible damage and future structural failures. It is generally carried out by leveraging the information obtained through monitoring processes which involves measuring the physical quantities to build a quantifiable understanding of the structure's current condition. The physical quantities, such as material characteristics, displacements, accelerations and strains, provide quantitative information about the condition of the civil structure or infrastructure. Therefore, they can be measured continuously to observe the structural integrity in real-time [2,3]. However, measuring these quantities is time-consuming, labor-intensive, complex, and costly. Moreover, the acquired measurements are highly dependent on the knowledge and experience of the person conducting the monitoring process.

Computer-vision and machine learning based techniques have been recently proposed to estimate the physical quantities and monitor the health of an entire structure or any specific member of a structure in a

* Corresponding author.
E-mail addresses: imran.waris@students.uettaxila.edu.pk (M. Imran Waris), vplevris@qu.edu.qa (V. Plevris), junaid.mir@uettaxila.edu.pk (J. Mir), N.chairman@westminster.ac.uk (N. Chairman), afaq.ahmad@uettaxila.edu.pk (A. Ahmad).

https://doi.org/10.1016/j.conbuildmat.2022.126899
Received 14 November 2021; Received in revised form 2 February 2022; Accepted 16 February 2022
Available online 16 March 2022

cost-effective and reliable manner. One of the available strategies involve the use of IP, ANN and ANFIS (adaptive neuro-fuzzy inference system) to predict the material characteristics through information obtained from images [4,5]. Such techniques employ digital cameras for vision-based inspection and monitoring [6] and model correlation criteria for damage identification in structures [7]. Damages in the structures are due to unanticipated loading, inappropriate shape or geometry of the member and flaws present in the material used [2]. Concrete, a compound of sand, fine aggregate, and coarse aggregate bonded together with cement, is arguably the most notable and widely used construction material in the world. Cement is the costliest material in the composition of concrete. Partly due to the increasing demand, production, and eventually use of cement, CO_2 levels in the environment are also on the rise [8]. To reduce the cost of cement, hybrid concrete (HC) is manufactured using waste materials [9] such as silica fumes (SF) and fly ash (FA) as replacements for cement. HC has several benefits: low production cost, reduction in CO_2, increased environmental sustainability, and long-term performance [10,11].

The main indicators of structural health and integrity have to do with the mechanical properties of concrete, primarily the compressive strength f_c and the tensile strength f_t. Several studies [12–19] have been performed on the mechanical properties of the concrete. The concrete properties can be quantified through conventional testing procedures, such as compression test according to ASTM C39 [20] and split-tensile test, according to ASTM C496 [21]. The techniques involved in these tests include core drilling, ultrasonic pulse velocity (UPV) [22], electrical resistivity measurement, and Schmidt hammer (SH) [23–26]. Based on the mode of their applications, the techniques for estimation of concrete properties can be classified into two main categories (i) destructive testing (DT) and (ii) non-destructive testing (NDT). A combination of DT and NDT can potentially reduce the error in measurements from 15% to 4% [23,26]. Several studies based on ANN and IP have been recently conducted to predict the mechanical properties of concrete [27–32]. Asteris et al. [33,34] estimated the compressive strength of concrete in an existing building through ANN utilizing the experimental results from two NDTs, UPV and SH. The compressive strength of concrete through ANFIS was predicted by Behnam et al. [35] using slump flow and the proportion of mixture as input. Haibang et al. [36] used an improved ANFIS model to predict the compressive strength of manufactured sand concrete, while Danial et al. [5] made a comparative study on estimating the compressive strength of cement-based mortar through ANN and ANFIS. Ahmad et al. [37] developed a ANN-based framework to estimate the load-carrying capacity of reinforced concrete (RC) structural members. Mansour et al. [38] developed an ANN model for predicting the shear strength of RC beams.

Basyigit et al. [39] estimated the compressive strength of concrete using IP, achieving an accuracy of 94.8%. The air gap feature of self-consolidating concrete was assessed through IP by Özerkan [40]. Lopez et al. [18] examined high-performance, lightweight concrete characteristics such as unit deformation, shrinkage, yield, and elasticity via image analysis. Nambiar and Ramamurthy [41] investigated the effects of shape, size, and volume of the air gap of foam concrete on its density and strength using the IP method. Dantas et al. [42] used an ANN model to estimate the strength of concrete mixed with construction and demolition scrap. Kim et al. [43] estimated the strength of concrete using a probability-based ANN model. Aworeya et al. [44] predicted the compressive and tensile strength of laterized concrete using ANN-based predictive models. Almashi et al. [45] proposed an ANN-based tool for the estimation of the strength and slump value of bentonite plastic concrete. Afaq et al. [46] developed ANN models to investigate the RC beam behavior in comparison with the physical models adopted by several concrete codes, including ACI, EC2 and JSCE, and found ANN to be a reliable tool for studying the response of RC beams.

Alshihri et al. [47] used ANN to estimate the strength of structural lightweight concrete exposed to a particular curing environment and evaluated ANN as a reliable method. Oreta and Kawashima [48] investigated the strength of confined concrete circular columns through ANN. Gupta [49] applied the ANN model to calculate the mixture for the normal pressure strength concrete. Moreover, compression tests were performed against different water/cement ratios of fiber-reinforced concrete to enable the ANN model to take into account the mixture characteristics. Gupta et al. [50] used parameters such as mixtures design, specimen shape, concrete size, environmental conditions, curing period, curing technique, etc., for ANN training and prediction to obtain an accurate estimation of the concrete strength. Compared to other methodologies, the adopted approach produced significant performance improvements in predicting the mechanical properties of concrete.

Yeh et al. [51] used ANN and second-order regression (SOR) to study the slump flow of high-performance concrete (HPC) and concluded that ANN is a more accurate model for the prediction of slump flow in comparison to second-order regression. Oztas et al. [52] predicted the strength and slump of high strength concrete containing several input parameters such as water to binder ratio, SF, FA, superplasticizers, air-entraining agent through neural networks. Cheng et al. [53] explored the relationship between a concrete slump and concrete components such as FA and slag using ANN. Bilim et al. [54] used ANN to predict the strength of blast furnace slag concrete. It was concluded that the shooting distance between the image of a concrete surface and the camera can affect the accuracy of the result. Liu et al. [55] performed regression analysis to develop a relationship between the shooting distance and the detection accuracy. They found that the accuracy in detection results through images decreases with the increase in the shooting distance. Celalettin et al. [39] used an IP technique to assess the compressive strength of concrete cubes after cutting them into four pieces and imaging the surfaces of the slices at the same height under fixed light intensity.

ANN and ANFIS are two of the most extensively used machine learning methods, having shown great ability of forecasting. These methods simulate, to some extent, the human brain processes. ANN emulates the connection between the neurons in the human brain and ANFIS uses both the human inference ability and the connection of biological neurons [56]. In structural engineering, these models are very useful for investigating the behavior of RC elements, vulnerability assessment of RC frames and predicting mechanical properties of concrete [57–60], among other applications in masonry structures [34,61] and other related fields [62]. One of the main advantages of neural networks is the possibility of considering various influential variables in the models and providing an appropriate estimation of the behavior of nonlinear and complex systems. Nasrin et al. [63] proposed a Bat algorithm based ANN model to predict the compressive strength of concrete. Armaghani et al. [5] presented a comparative study of ANN and ANFIS models for the prediction of the compressive strength of cement based mortar. Hosein and Mirrashid [64] introduced three bio-inspired ANN models to estimate the shear strength of RC beams with steel stirrups. Previously, these models have been developed using the quantities of the constituents of concrete as input values to determine the properties of concrete. In this article, ANN and ANFIS models have been formulated using statistical features extracted from concrete images through IP as input value to predict concrete properties. The pixel values of the concrete images provide information of the constituents of the concrete that can be related to its mechanical properties [39].

In the present work, a novel NDT technique based on IP, ANN and ANFIS is proposed for predicting the mechanical properties of hybrid concrete. Towards achieving this goal, 162 cylindrical concrete samples of varying compressive and tensile strengths were manufactured, first using different mix ratios (MR). For this purpose, cement replacement material (CRM), water-cement (W/C) ratio, water content (WC), compaction, and curing time were varied during sample manufacturing. Three identical concrete samples were prepared against each mix ratio. Two of these samples were utilized in conventional compression and split-tensile destructive tests to get the ground-truth compressive and tensile strengths of the material. The third identical concrete sample was

cut into three slices for image processing and acquisition. Statistical features from the acquired concrete slice images were then extracted to train and test the ANN and ANFIS models for predicting the concrete compressive and tensile strength using images only. The predicted values by ANN and ANFIS were compared with the ground truth experimental values obtained with the destructive tests. The proposed NDT technique results were also compared with other NDT methods such as SH and UPV.

The remainder of the paper is organized as follows: Section 2 introduces IP, ANN, and ANFIS. Section 3 discusses conventional destructive tests (CDT) and the specimens' preparation, testing, and cutting procedures. Section 4 elaborates the proposed method based on image processing artificial neural network (IPAN) that includes the processing of images and training of ANN and ANFIS models. The results of the research are presented in Section 5, while Section 6 includes the conclusions of the study.

2. Image processing, artificial neural network and adaptive neuro-fuzzy inference system

Image processing is about processing an image using computer algorithms to extract useful information. Several software packages, such as MATLAB, ImageJ, and specialized Python libraries [65–67], have been successfully utilized to process images. An image file can be transformed into a digital form through an image processing technique called digitalization. In a digitized image, each element of the matrix represents a pixel. A pixel, the basic logical element of the image, reflects the brightness of the unit area of a grayscale picture [68]. Image processing techniques include image digitalization, image quality enhancement, segmentation, classification, image recognition, and pattern recognition. In aeronautics and aerospace, image processing is used to process satellite images, in biology and medicine to evaluate biomedical images, in engineering and physics for processing spectrometric images and electron microscopy [69]. The matrix acquired through image processing can be used in conjunction with ANN to resolve problems.

Artificial neural network is an algorithm inspired by the human brain to deal with complex and time-consuming problems. The computer algorithm can carry out duties similar to the ones of the human brain, such as learning, making decisions, recalling and concluding. ANN can learn from input and output data and can model the relationship between them, based on which it can be asked to predict new outputs on unseen input data. Although ANNs show analogies to only some of the human brain's operations, they were originally inspired and established by modeling the structure of the brain. In an ANN structure, there is usually one input layer, one output layer, and one or more hidden layers (HL) [70].

ANFIS combines two separate computational techniques, namely the ANN and the fuzzy inference system (FIS). ANFIS provides the ANNs with the ability to learn from the data and develop and use the relationship between input and output data through fuzzy rules [71]. In this hybrid technique, first, the inputs and outputs of the dataset are introduced to the algorithm to derive the input of the initial fuzzy model using fuzzy rules. Next, the ANN is utilized to improve the derived fuzzy model to develop the final ANFIS model for the provided data. The architecture of the ANFIS model contains five layers and a membership function (MF). The MF of the ANFIS is a curve that reads the gap of an input value from 0 and 1 in the input data [71,72]. The first layer is the input layer that controls the position of the fuzzy set, and input values are introduced to the model through it. The input values are transferred to the second layer after the application of the MF. The second layer in the model determines the degree of activation of the fuzzy rule and computes the input for the third layer through fuzzy input. The nodes in the third layer normalize the extent of activity of the fuzzy rule. In the fourth layer, fuzzy "if-then" rules are applied to the output values of the third layer. The fifth layer is the output layer which is represented by Σ, denoting the summation of the values of the fourth layer. The nodes in the ANFIS model are of two types, adaptive and fixed nodes. Layers 1 and 4 contain adaptive nodes that are depicted as square boxes. The other layers in the model have fixed nodes represented by circular boxes [5,72]. In the proposed study, the ANFIS model is adopted to estimate the compressive and tensile strength of hybrid concrete.

3. Sample production and testing

In this section, details about the materials and mixing used in the preparation of the concrete cylindrical samples are presented. Then, the procedure followed in the image acquisition stage is elaborated. Finally, details of different DT and NDT techniques utilized in this study are given.

3.1. Sample preparation

162 cylindrical concrete samples with dimensions 150 mm (diameter) × 300 mm (height) were prepared. It is well known that the final mechanical characteristics of concrete are affected by several parameters. In this study, 9 mix designs with three different percentages of replacement (0%, 15%, 25%) of SF and FA were considered. In each mix design, 6 parameters were taken into account, namely: MR, W/C ratio, aggregate quantity, compaction method, curing age, and use of CRM. The whole procedure from the casting of specimens to the imaging of slices is depicted in the flowchart of Fig. 1. Three classes of the samples with replacement (R) of cement with 0%, 15%, and 25% of SF and FA and their subclasses are given in Table 1. Each MR for sample preparation was given a unique name. The nomenclature of the samples is as described in the following example: "10S0.4WC", where 10S is the sum of MR component (1 + 3 + 6), 0.4WC shows the W/C ratio, and the last part, (0C, 15C or 25C), whenever present, shows the percentage of CRM (0%, 15% or 25%). To observe the effect of each variable on the properties of concrete, a sufficient number of concrete samples were produced.

The water/cement ratio is a significant parameter for concrete mainly because of its role in concrete's surface appearance and the number of voids in concrete. In the present study, three W/C ratios (0.4, 0.5, and 0.6) have been used in the production of the samples, as described in Table 1. The water used was according to the ASTM C 94 [73] and ACI 318 [74] requirements. Besides that, three different cement dosages were chosen. It was expected that the color of concrete will differ, depending on the change in the cement dosage. CRM decreases the void ratio and fluidizes concrete according to ASTM 31 [75]. During the fabrication of the 81 specimens, FA and SF were used as CRM in 54 samples. The specifications of cement and the CRM used are given in Table 2.

54 specimens, one sample, identical to the others from each class, were selected for the photography. A schematic diagram of the cutting to be done with a cutting saw is shown in Fig. 1. Every sample opted for the photography was cut into three equal pieces of approximately 100 mm (height) each, to study the effect of the aggregate distribution on the mechanical characteristics of concrete. If samples were not cut and only images of the top surface were utilized, the results would be misleading due to the accumulation of fine material on the top concrete surface [39,76]. Therefore, the parameters influencing the concrete's mechanical characteristics, such as the feature of cement paste, void ratio, aggregate distribution, etc., were observed at each face of the sample slice. The cutting scheme of samples to acquire concrete slices is depicted in Fig. 2. The cutting of the samples was done with a stone cutting saw. The top and bottom faces of the slices for a particular sample are shown in Fig. 3.

3.2. Image acquisition setup

A special small room (2.00 m by 2.50 m) was designed, built and

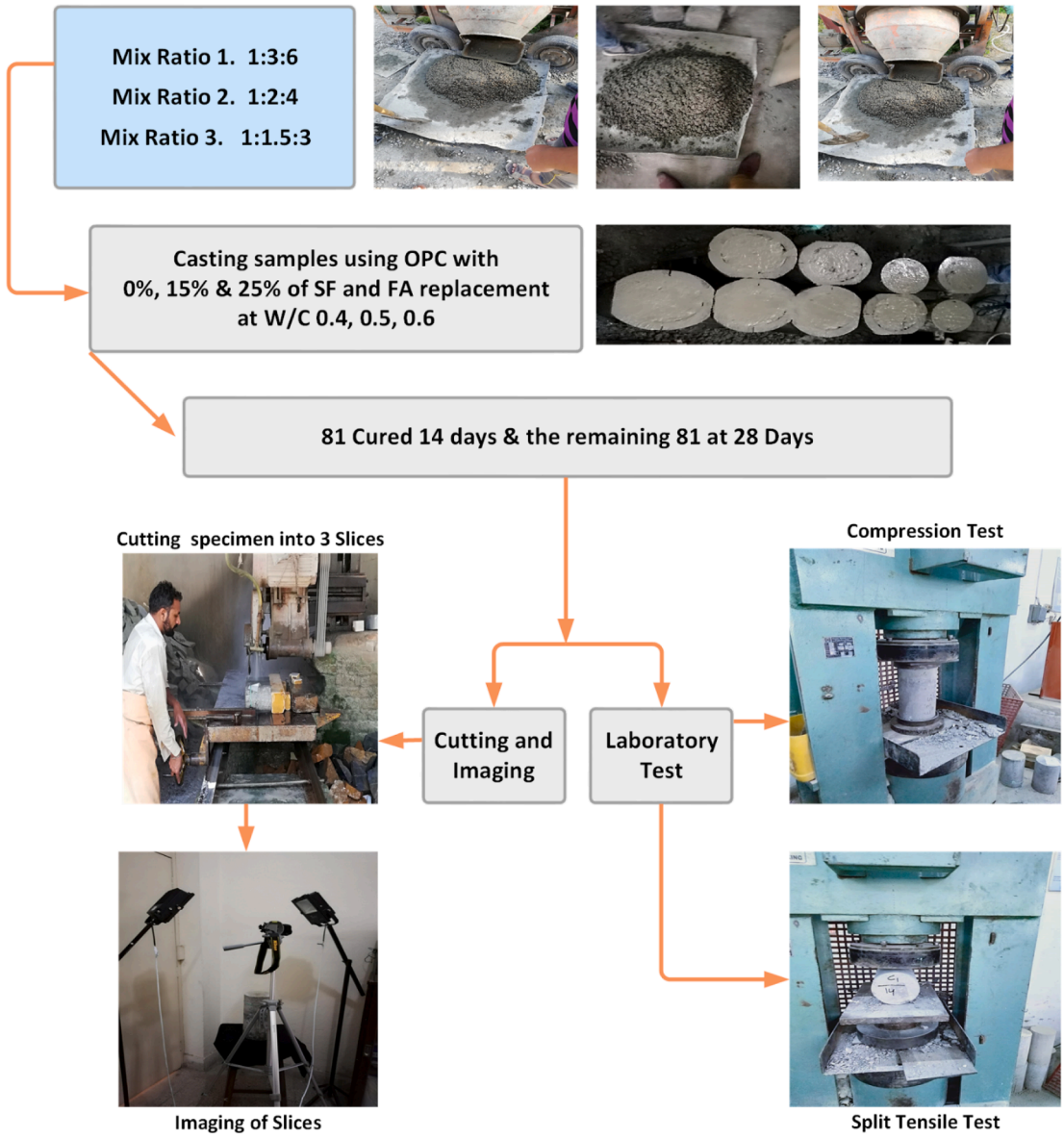

Fig. 1. Flowchart of the process from casting to performing laboratory tests and imaging.

used for generating the image acquisition setup for taking the prepared concrete slice sample images. Since the efficiency of image processing techniques is largely dependent on the quality of the obtained images, the images need to be acquired in a fully controlled environment. For this reason, special arrangements were made to ensure that the acquired images of the cylinder slices will be free of light variations, shadows and noise. To this end, the sunlight was first fully blocked by using special black sheets on each entry point of light in the room. The cylinder slice samples were then illuminated from a specific direction and angle by two 30 W LED bulbs that produced an artificial light of 2000 lx measured through a lux meter (Lutron LX 1109) [68]. The use of artificial lighting ensures uniform illumination in the room and that the captured images will be as free of unwanted shadows as possible. A digital camera with 24 megapixels resolution (Nikon DSLR 3300) was used for the imaging. The ISO value, which is generally known as the camera's sensitivity to light, was kept constant at 1000. The camera was mounted on a stand, and images were captured directly from the top with a fixed distance of 600 mm between the camera and the sample slice surface. The collected images had a 6000 × 4000 pixels resolution. The complete image acquisition setup is depicted in Fig. 4 (a).

3.3. Destructive testing (DT)

The destructive tests were performed to obtain the mechanical characteristics of concrete through conventional methods. The compression test and split-cylinder tests were performed on hardened concrete to examine the behavior of concrete samples under compressive and tensile loading. Besides DT, NDT techniques such as SH and UPV tests were performed on the cut slices.

3.3.1. Compressive strength

The prepared cylindrical concrete samples of HC containing CRM FA and SF replaced by 0%, 15%, 25% against the weight of cement were examined through compression test to acquire the value of the compressive strength f_c. The compressive strength of hardened concrete was measured according to ASTM C39 [20] depicted in Fig. 4 (b). The obtained values of f_c are represented in Fig. 5.

The pozzolanic action (PA) of FA and SF generates supplementary calcium silicate hydrate (CSH), which contributes to the strength of HC. The increase in the compressive strength at a later age is because the pozzolanic action of FA starts late while the one of SF starts at an early

Table 1
Three classes of samples and their subclasses. Compressive and tensile strengths are reported at 14 and 28 days, as averages of 3 specimens (tests), per case.

Mix Design	Mix Ratio	W/C Ratio	CRM	CRM	f_c (MPa)		f_t (MPa)	
			FA (%)	SF (%)	14 Days	28 Days	14 Days	28 Days
0% Replacement (R)								
10S0.4WC	1:3:6	0.4	0	0	13.44	16.94	4.28	4.55
10S0.5WC	1:3:6	0.5	0	0	10.81	12.07	3.24	3.51
10S0.6WC	1:3:6	0.6	0	0	10.2	11.96	3.54	5.43
7S0.4WC	1:2:4	0.4	0	0	13.71	16.56	8.5	8.28
7S0.5WC	1:2:4	0.5	0	0	10.86	14.7	4	6.53
7S0.6WC	1:2:4	0.6	0	0	11.24	14.32	3.84	4.39
5.5S0.4WC	1:1.5:3	0.4	0	0	15.74	16.02	4.39	5.83
5.5S0.5WC	1:1.5:3	0.5	0	0	13.55	15.9	3.57	4.06
5.5S0.6WC	1:1.5:3	0.6	0	0	13.82	14.81	3.51	4.33
15% Replacement (R)								
10S0.4WC	1:3:6	0.4	15	15	13.91	15.25	8.23	8.78
10S0.5WC	1:3:6	0.5	15	15	11.24	14.1	6.47	8.12
10S0.6WC	1:3:6	0.6	15	15	10.1	13.6	4.39	4.55
7S0.4WC	1:2:4	0.4	15	15	14.7	16.75	5.76	6.42
7S0.5WC	1:2:4	0.5	15	15	13.99	16.13	3.4	4.11
7S0.6WC	1:2:4	0.6	15	15	13.44	14.7	4.17	5.02
5.5S0.4WC	1:1.5:3	0.4	15	15	17.8	16.02	5.92	6.31
5.5S0.5WC	1:1.5:3	0.5	15	15	17.1	15.9	5.2	6.4
5.5S0.6WC	1:1.5:3	0.6	15	15	15.91	14.81	5.5	6.53
25% Replacement (R)								
10S0.4WC	1:3:6	0.4	25	25	13.99	16.78	8.75	7.91
10S0.5WC	1:3:6	0.5	25	25	12.89	14.92	6.58	6.28
10S0.6WC	1:3:6	0.6	25	25	10.81	14.43	5.46	4.86
7S0.4WC	1:2:4	0.4	25	25	20.57	23.2	6.91	6.47
7S0.5WC	1:2:4	0.5	25	25	17.61	18.54	5.16	5.54
7S0.6WC	1:2:4	0.6	25	25	18.04	18.21	9	6.47
5.5S0.4WC	1:1.5:3	0.4	25	25	24.35	27.09	7.19	5.27
5.5S0.5WC	1:1.5:3	0.5	25	25	21.39	21.83	7.29	9.87
5.5S0.6WC	1:1.5:3	0.6	25	25	16.84	21.05	6.2	5.27

Table 2
Specifications of cement and CRM.

Chemical composition (%)	Cement	Silica fume	FA
Silica	22.5	84–86	57–65
Aluminum oxide	5	1.0 (max.)	28–32
Iron oxide	4.0	2.0–3.5	1–4
Calcium oxide	64.25	1.0–1.5	1–2
Loss on ignition	0.64	4–7	9.01

age [77,78]. The compressive strength of concrete with SF and FA was low at an early age, but a significant increase was noticed in a specimen of 28 days. At 14 days age with 0% of SF and FA and W/C 0.6, the compressive strength of the specimen is 13 MPa, while a similar specimen with 25% of SF and FA has a compressive strength of 17 MPa. The same trend can be noticed for other mix ratios. The obtained results reveal that the replacement of cement with SF and FA has a positive effect on the strength of HC. The rise in the strength of concrete was rapid with the increase in the SF content.

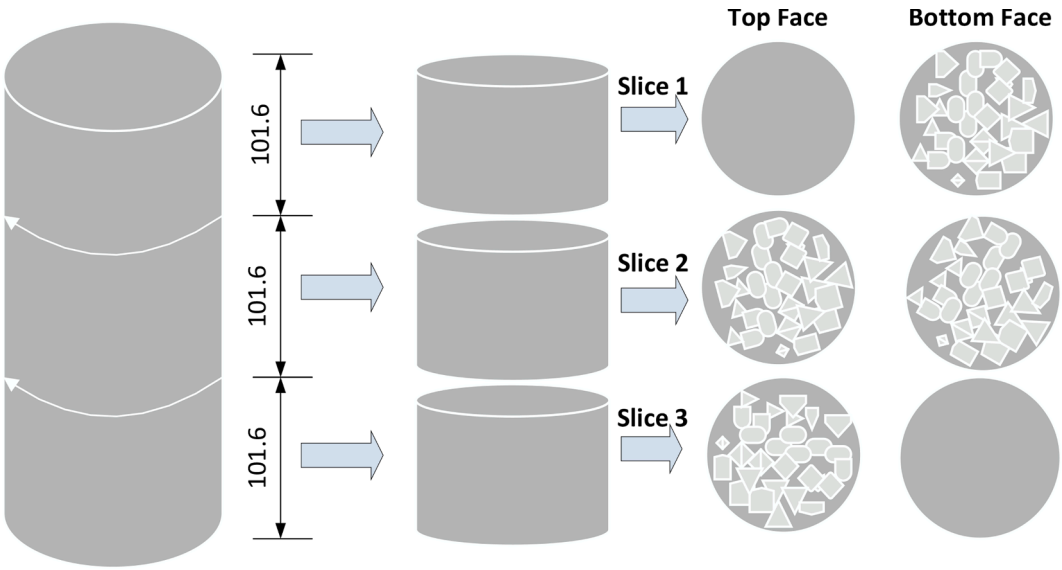

Fig. 2. Schematic representation of the cutting of a sample into three slices.

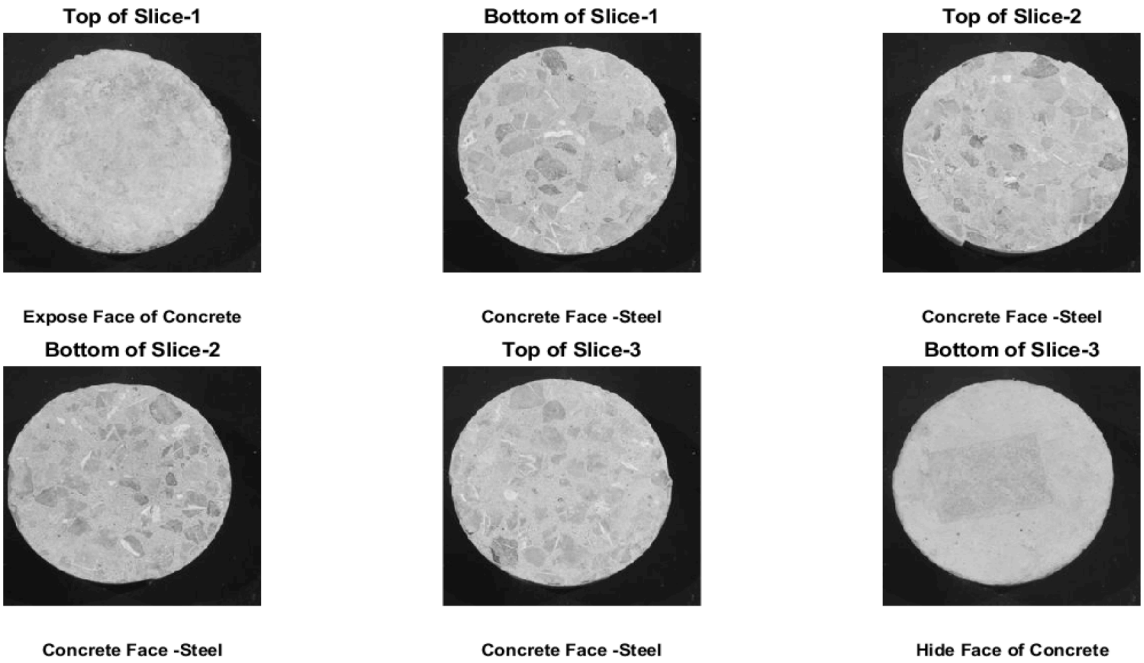

Fig. 3. Three slices of a sample with their photographed (top and bottom) faces.

Fig. 4. Laboratory tests, (a) Image processing setup, (b) Compression test, (c) Split-Tensile test.

3.3.2. Split-Tensile strength

The split tensile test was performed according to the ASTM C496 [21] standard test method shown in Fig. 4 (c). The experimental values of the tensile strength are presented in Fig. 6, where it can be observed that the split tensile strength of the cylindrical sample with 0% of CRM is low compared to the samples containing CRM. The increase in split tensile strength is because of the improved interfacial bond, which was attained by replacing cement with SF and FA, which are finer materials compared to cement [79].

3.4. Non-destructive testing (NDT)

3.4.1. Schmidt hammer

After the imaging of the samples, the surface of the slices was made smooth and the Schmidt hammer test was conducted on each slice according to ASTM C805 [80]. The obtained *R*-value was used to calculate the compressive strength of the slices. Fig. 7 shows the compressive strength obtained from the SH test.

3.4.2. Ultrasonic pulse velocity

UPV test was performed on the slices according to [81]. The time travel of 250 kHz frequency waves through the slice was obtained and the value of the velocity was calculated from the formula given in Eq. (1), where v is the velocity, T is the thickness of the concrete slice, and t is the time of travel of the ultrasonic wave. Then, based on the speed, the UPV-based compressive strength is estimated. The corresponding results are presented in Fig. 8.

$$v = T/t \tag{1}$$

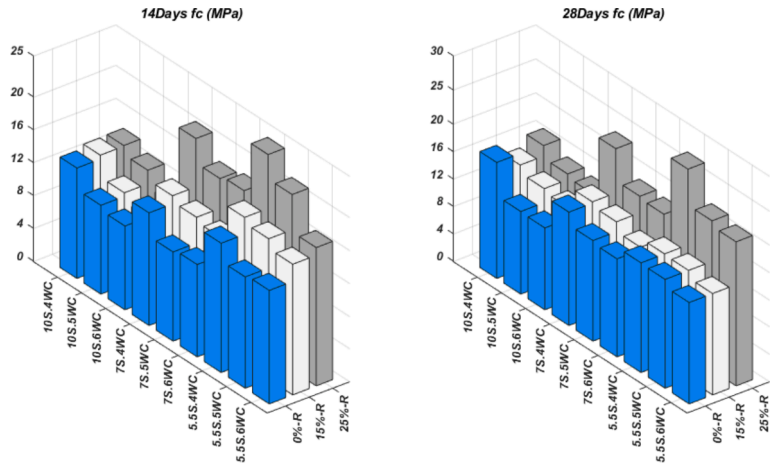

Fig. 5. Graphical representation of compressive strength: (a) at 14 days, (b) at 28 days.

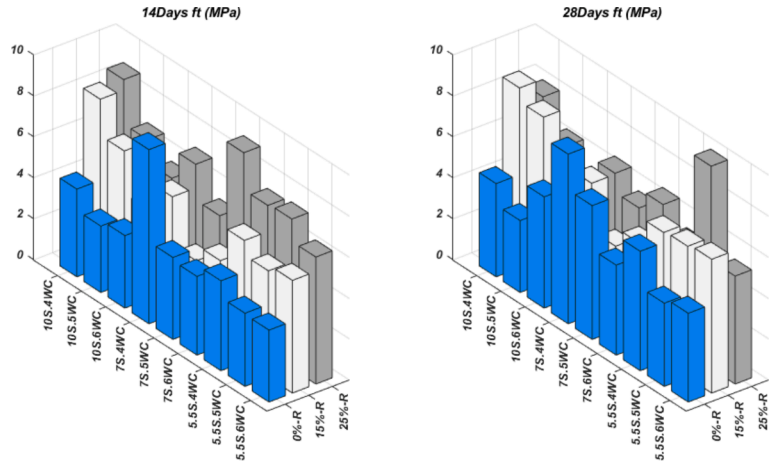

Fig. 6. Graphical representation of the tensile strength: (a) at 14 days, (b) at 28 days.

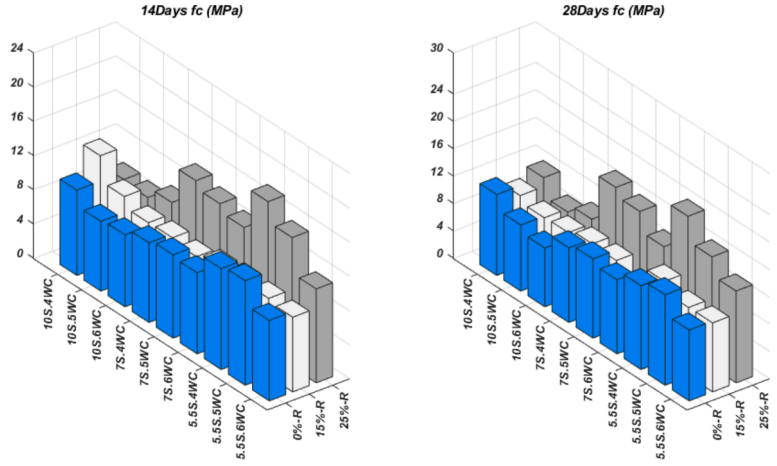

Fig. 7. Graphical representation of the compressive strength obtained from the Schmidt Hammer test: (a) at 14 days, (b) at 28 days.

4. Proposed method (IPAN)

4.1. Image processing of samples

Using a MATLAB-based image processing tool, the acquired images of concrete slice samples were transformed into matrix form of size 4000×6000 in accordance with the resolution of the image (24 Megapixels). Images were cropped to contain only the concrete portion. The original images were true color images (RGB images). The RGB images were converted to grayscale format by creating a weighted sum of the R (red), G (green) and B (blue) components using Eq. (2),

$$GS = 0.298 \times R + 0.589 \times G + 0.113 \times B \quad (2)$$

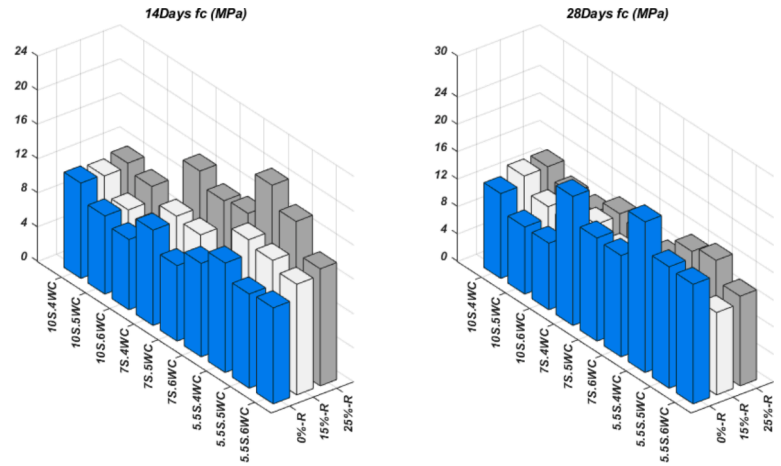

Fig. 8. Graphical representation of the compressive strength obtained from UPV: (a) at 14 days, (b) at 28 days.

where *R*, *G* and *B* represent the red, green and blue color component of a pixel and *GS* is the calculated grayscale component. The grayscale images were then resized to a smaller size of 256 × 256 pixels. Pixel values of the matrix represent the appearance of the concrete sample and the brightness at a point in an image and produce an input segment of ANN. Statistical features, namely, the arithmetic mean, standard deviation and median, third moment, skewness, and entropy, were calculated to reduce ANN processing time and increase the accuracy of the prediction [68,82,83]. A description of these features is given in Table 3 and their mathematical formulas are given in Eqs (3)–(8) [84].

$$M = \frac{1}{k}\sum_{i=1}^{k} \mathrm{V_i} \tag{3}$$

$$Me = \{(k+1) \div 2\}^{th} \tag{4}$$

$$Std = \sqrt{\frac{1}{k}\sum_{i=1}^{k} (V_i - M)^2} \tag{5}$$

$$Mo = \frac{1}{k}\sum_{i=1}^{k} (V_i - M)^3 \tag{6}$$

$$E = -\sum_{i} p_i{*}\log_2\left(p_i\right) \tag{7}$$

$$\mathrm{Sk} = \frac{\frac{1}{k}\sum_{i=1}^{k}(V_i - M)^3}{Std^3} \tag{8}$$

where *M* denotes mean value, *k* is the total number of data values for the variable, V shows the variables in the digitized matrix, *Me* is the median value of the pixels in the digitized pictures, *Std* denotes the standard deviation, *Mo* denotes the third moment, *E* is the entropy, *p* contains the normalized histogram counts, and *Sk* is the skewness value.

The matrix size was further reduced to 6 × 256. The 6 × 256 matrix contains six rows and 256 columns, where the rows contain the mean, standard deviation, median, third moment, skewness and entropy, respectively, for every image of the sample. For six images of the concrete sample, a combined matrix (CM) of 6 × 256*6 (6 × 1536) was obtained. The CM has 1536 matrix values of the mean, standard deviation and the other statistical features for every specimen. The histogram diagrams for six images of a concrete sample are shown in Fig. 9. The histogram represents the distribution of the color values of each color in the numerical image. By observing the histogram of the top face of the image specimen, it was noted that pixels are well distributed in the images. Similarly, the pixel distribution (PD) in images of the remaining specimens was observed. The histogram of the above-mentioned figures also contains a black region, so images were cropped at the center portion and the distribution of pixels in the histogram of the cropped region was observed.

In Fig. 10, the histogram of the top faces of images of the specimen with MR 1:03:06 shows the effect of W/C and CRM on PD. The relationship between the compressive strength of concrete and its surface appearance can be noticed in the graphs. Also, the effect of the camera distance from the surface of the sample and the effect of FA and SF on air voids can be observed.

In addition to the histogram bars distribution depending on the availability of aggregate, air gap and amount of cement and sand on the cut surfaces, masking was also performed to obtain only the concrete related portion of the image after removing the non-concrete portion. Masking was done using the thresholding technique of image processing technology. The image was divided into two areas, white and black, with pixel values "1" and "0", respectively, with white representing the concrete area and black the remaining (non-concrete) part of the image. The resultant image was obtained as the input for the ANN. The original image and its mask are shown in Fig. 11.

Table 3
Statistical features.

Feature	Expression	Description
Mean	*M*	Measure of average intensity
Median	*Me*	Middle value of pixel in an ordered column
Standard deviation	*Std*	Measure of average contrast
Third moment	*Mo*	Measure of the distribution skewness
Entropy	*E*	Measure of randomness in pixels
Skewness	*Sk*	Measure of asymmetry in matrix

4.2. Ann modelling

The input data produced from the matrix acquired through image digitalization was then used for the ANN training. The outputs of the ANN used for its training are the f_c and f_t values obtained from the laboratory tests. Both input and output data were normalized to a range between 0 and 1 using Eq. (9), where *N* denotes the normalized value of the variable V, while $\mathrm{V_{min}}$ and $\mathrm{V_{max}}$ are the lowest and highest values of the variable V, respectively.

$$N = \frac{(\mathrm{V} - \mathrm{V}_{min})}{(\mathrm{V}_{max} - \mathrm{V}_{min})} \tag{9}$$

The architecture of the ANN with one input layer, two hidden layers (HL), and one output layer is shown in Fig. 12. The number of hidden

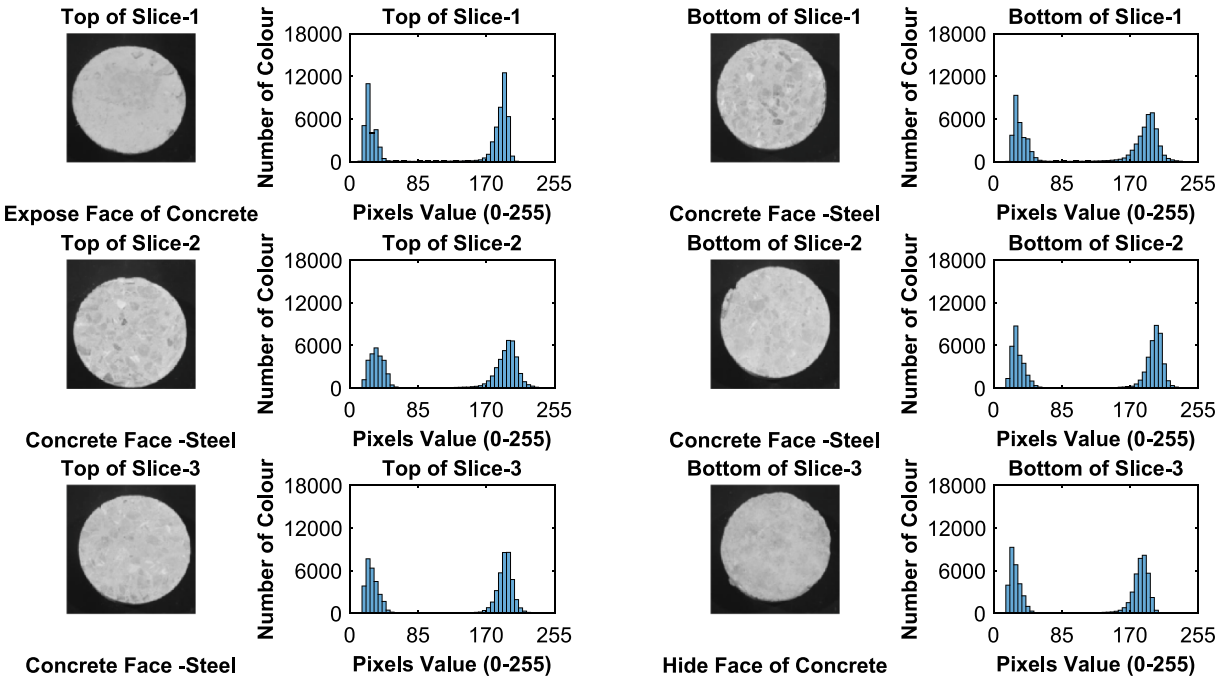

Fig. 9. Histograms of three slices of a concrete sample at 600 mm.

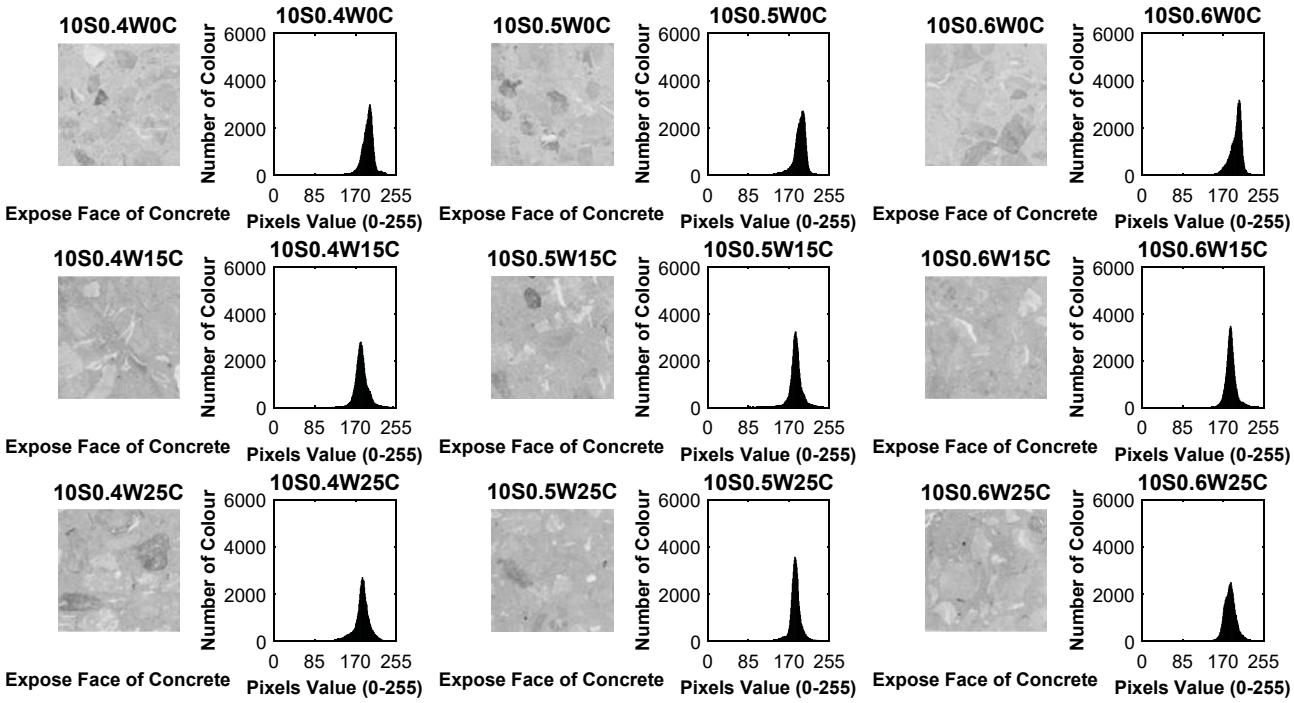

Fig. 10. Histogram of top faces of MR 1:03:06 against different W/C and CRM at 600 mm.

layers (2 in this case) was selected based on the experience of the authors and on several trial-and-error attempts in order to optimize the network performance. 6 nodes were also determined suitable for each hidden layer as a result of these trial attempts. The number of nodes for the input layer and output layer vary based on the given parameters of inputs and outputs in the data set. These are kept to a minimum to reduce the processing time, as extra calculations caused by the neurons and the weight vectors in any layer can increase the processing time. The output layer consists of two nodes, based on the targeted mechanical properties of the concrete (i.e. the f_c and f_t values).

The Levenberg-Marquardt back-propagation (LM-BP) supervised learning algorithm [85,86] is one of the most powerful and widely used training algorithms which has been used in the present study for the ANN training. The logarithmic function was employed as the nodes under constant learning values (*lr*) and learning ratio values under constant hidden nodes were changed in both the HL. An optimal ANN structure can be considered as the one corresponding to the lowest error value. The learning value is a common parameter that updates the weights to minimize the loss function of the network and affects the speed of the ANN process. Another significant parameter for the

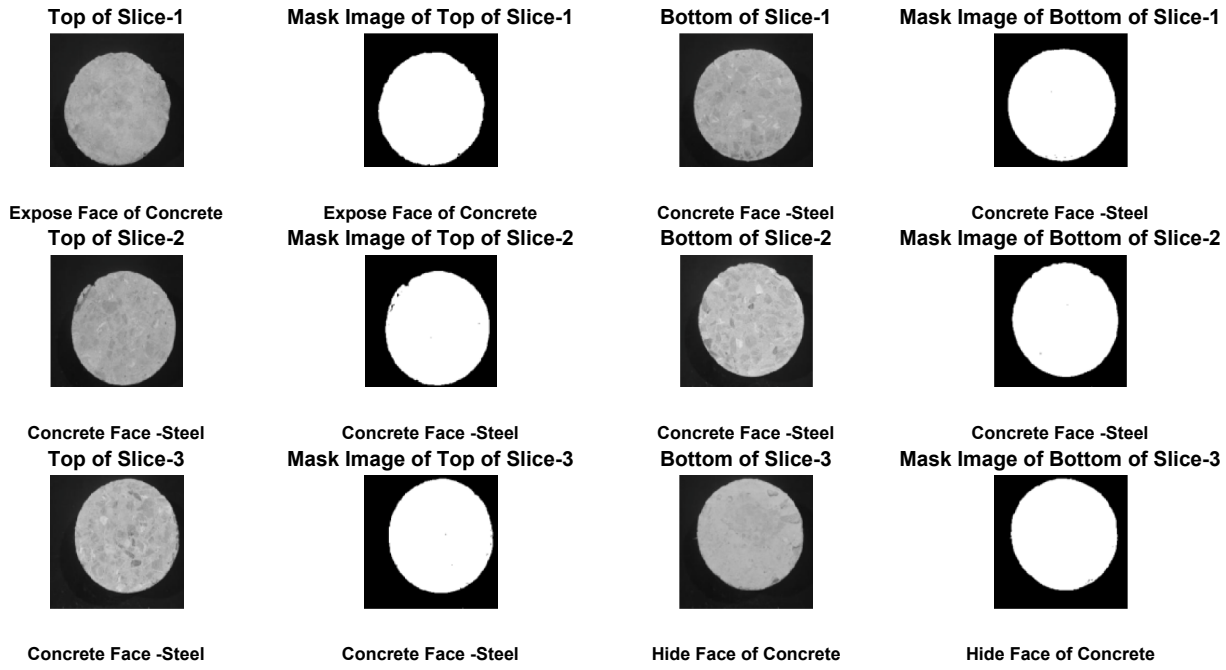

Fig. 11. Six faces of three slices of a concrete sample with the mask image.

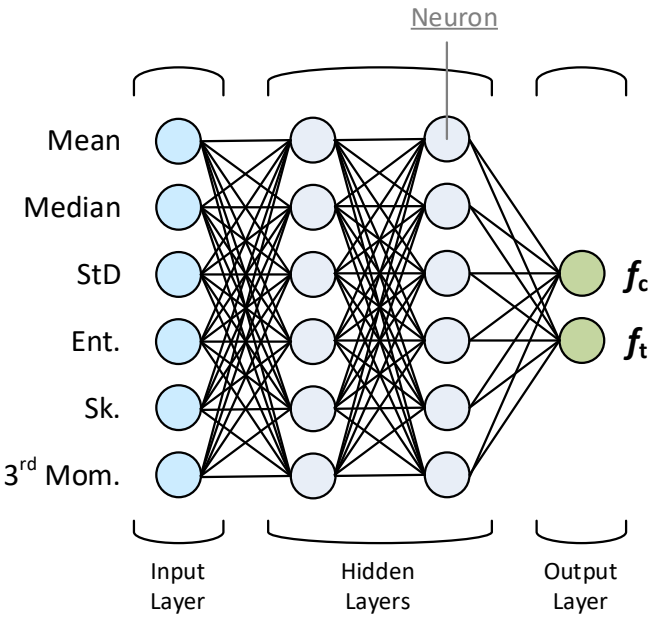

Fig. 12. Architecture of the optimal ANN model (6-6-6-2).

performance of the network is the moment constant (*mc*) which is also user-defined. There is no general rule for the selection of these parameters for an ANN. In this study, the maximum number of iterations was set to 10000, while $lr = 0.9$ and $mc = 0.2$ [68,87–89]. In this study, different ANN models have been used. All ANN models share the same activation functions (i.e., log sigmoid and Hyperbolic tangent functions) between the layers. Their difference lies in the network architecture, i.e. the number of hidden layers and the number of neurons in each of them.

After normalization of the data (statistical features, DT values), several ANN models of the LM-BP algorithm were trained, tested and validated by varying the number of HL and HN for every model, while the number of neurons in the input and output layers were kept constant. The optimal ANN model was the one with 2 hidden layers each having 6 neurons, exhibiting the minimum training and testing error. The formula for calculating the error for training and testing is given in Eq. (10) and it is usually expressed as a percentage (%).

$$ET = \frac{1}{j}\sum_{m=1}^{j} |D(m) - E(j)| \tag{10}$$

In the above formula, $D(m)$ denotes the output (target) values, $E(j)$ denotes the ANN predicted values and j is the number of data points in the model.

4.3. Training and testing

For the training, validation and testing of the proposed method, relevant features extracted from 324 images of 54 samples and values from experimental tests were used. The training and testing process were carried out using features either individually, in a combination of two, or using all three together. The total dataset was divided into three parts, with 70% of the data used for training, 15% for validation, and 15% for testing purposes. The output from the ANN and ANFIS model was determined as the value of the compressive and the tensile strength, respectively, from each output node, as shown in Fig. 12. Results obtained from the training and testing of the ANN and ANFIS model were compared with the laboratory results for the 54 samples and the NDT performed on slices. Fig. 13 depicts the steps followed from the casting of the specimen until the training of the ANN and ANFIS model.

4.4. ANFIS modelling

Similar to ANN, Adaptive Neuro-Fuzzy Inference System (ANFIS) can be used to solve complex engineering problems. ANFIS is also a powerful tool for predictions by building a relationship between input and target values. The architecture of ANFIS contains five principle layers described as fuzzyfing layer, implication layer, normalizing layer, defuzzyfing layer, and combining layer [5,90]. The optimized ANFIS model was achieved by adjusting the five respective parameters of ANFIS, namely the type of input fuzzy sets, the membership function, number of epochs, type of output membership function and optimization technique.

In this study, ANFIS models with three membership functions, namely Generalized bell-shaped, Triangular, and Gaussian MFs (*gbellmf*,

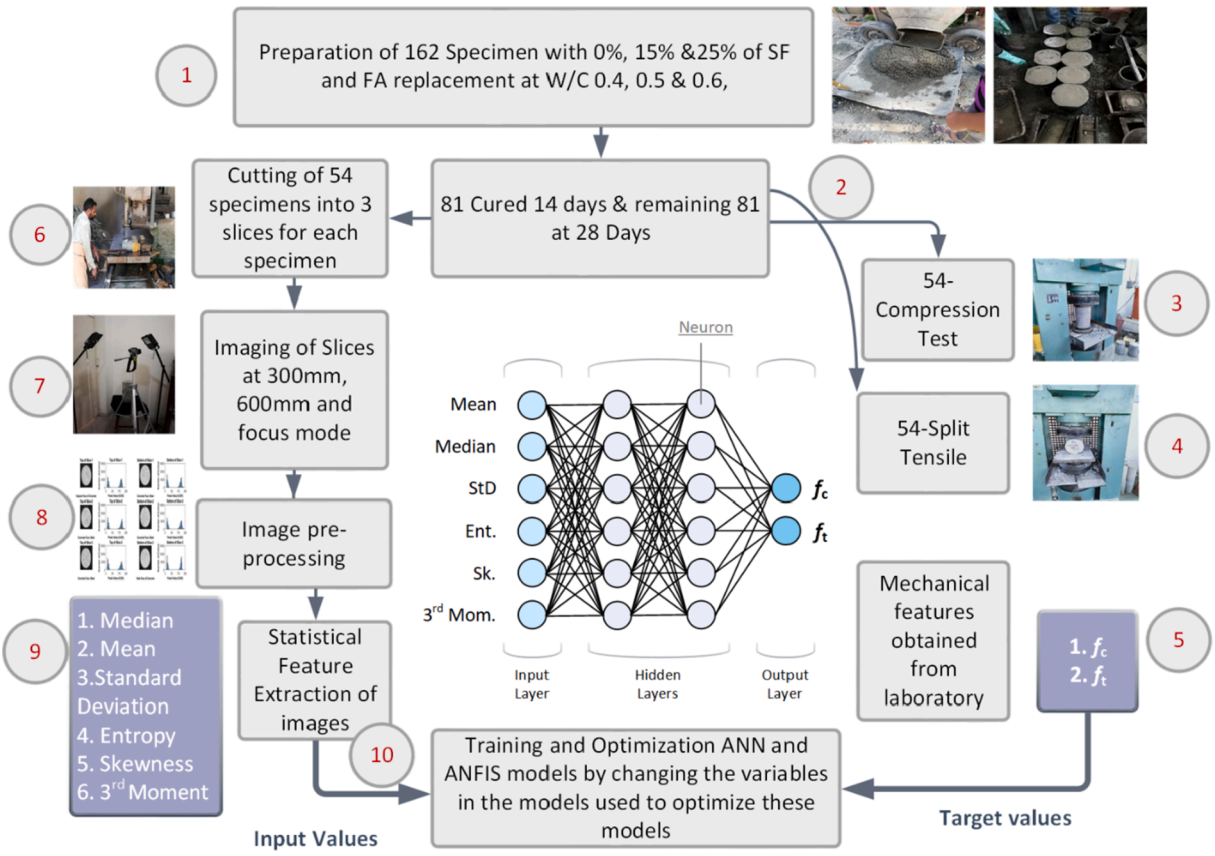

Fig. 13. Flowchart depicting the step-wise process from casting of samples to ANN training.

trimf, *gaussmf* commands in MATLAB, respectively) were used with randomly varying number of epochs between 50 and 200. The mathematical representations of the membership functions are given in Eqs. (11), (12) and (13).

$$trimf(u,a,b,c) = max(\min\left(\frac{U-a}{b-a}\right), 1, \left(\frac{c-U}{c-b}\right) \tag{11}$$

$$gaussmf(u,c,\sigma) = e^{-\frac{1}{2}\left(\frac{U-c}{\sigma}\right)^2} \tag{12}$$

$$gbellmf(u,a,b,c) = \frac{1}{1+\left|\frac{U-c}{a}\right|^{2b}} \tag{13}$$

where U is the input value and a, b, and c are parameters of the membership functions to determine width, tip and locate center of the curve for Eqs. (11) and (13). In Eq. (12), σ determines the width of the curve. The ANFIS model with triangular MF showed accuracy of 91.43%, while accuracy of 94.24% was obtained for the Gaussian MF model. The optimized ANFIS model was the one obtained at epoch 100, with the use of the Generalized bell-shaped (*gbellmf*) membership function, achieving accuracy of 96%. The input number of the membership functions was also changed to achieve optimization. The curves with input value between 0 and 10 for the three MFs [91,92] applied in this study are presented in Fig. 14.

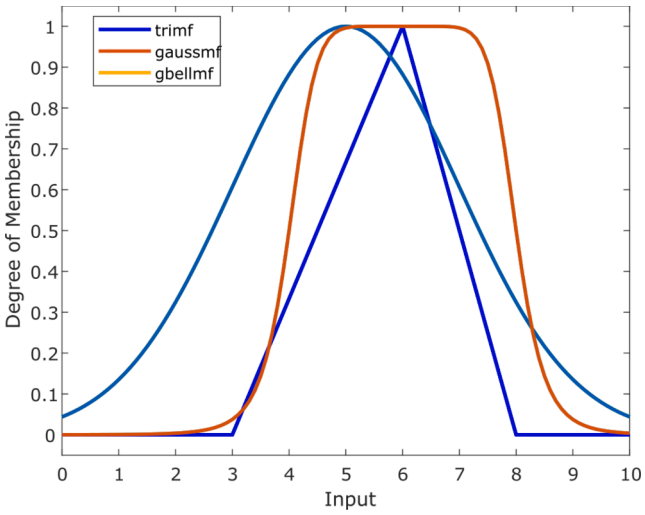

Fig. 14. Curves of the ANFIS membership.

5. Results

In the present study, an amalgam of three artificial intelligence techniques, namely IP, ANN and ANFIS, in two ways were applied to determine the mechanical characteristics of concrete. In the first one, IP and ANN were properly combined, while the second one consists of a combination of IP and ANFIS. 54 × 3 = 162 specimens of HC were produced with three identical samples in each mix ratio. One set of the identical samples (54 pieces) was selected for the compressive laboratory testing (f_c), another one (54 pieces) for the tensile laboratory testing (f_t), and the last one (54 pieces) for the digital photography. The experimental results and the results from the adopted method were compared and found similar. The results from tests and the adopted method can be compared as follows.

Numerous factors can affect the mechanical properties of concrete. A data set could be produced including most parameters such as water/cement ratio, curing, CRM, the quantity of cement, compaction, size of aggregate, size, and shape of the specimen. The specimens of the hybrid concrete which contained 25% CRM (SF and FA) showed better strength

compared to the specimens with 15% or 0% CRM. In a similar manner, the samples with 15% CRM showed better results than the samples with 0% CRM. This effect in the strength was due to enhanced PA because of the presence of SF and FA.

The size and range of data set affect the outcomes of an ANN model. In this study, $54 \times 2 = 108$ concrete cylinders with different parameters such as water/cement ratio, CRM, curing (14 days, 28 days), compaction etc. were used. The experimental results obtained from the specimens vary between 10.1 MPa and 27.09 MPa for compressive strength and 2.19 MPa to 9.87 MPa for tensile strength.

An ANN model with 2 hidden layers and 6 nodes in each hidden layer was employed, while the parameters *lr* and *mc* were taken equal to 0.9 and 0.2, respectively. The chosen parameters affect the performance of ANN such as processing time, accuracy, among others. The most preferred values of the effective parameters for ANN used by researchers are favored. The regression values obtained from the trained ANN models and the different ANFIS models are reported in Table 4.

The results of regression values at the overall stage obtained from the optimized (IP, ANN) model, with R = 99.7%, and (IP, ANFIS) model, with R = 97.8%, are also depicted in Fig. 15 and Fig. 16, respectively. At this point it has to be noted that different combinations of parameters are used mainly because of their effect on the mechanical properties of concrete. Therefore, the obtained results are specific to the parameters used and this can be considered as a limitation of the study.

Moreover, it was noticed that the mechanical properties of concrete are affected by the mix ratio, WC, and the amount of replacement (SF, FA) used to produce a specimen. Mix ratio 10S with 0.6 WC, 0% R, and 14 days of curing showed lower f_c and f_t values of 10 MPa and 3.5 MPa, respectively. The specimens of the same MR with a rise in the percentage of R, curing age, and reduction in WC showed enhanced f_c and f_t values. It was observed that the increase in the amount of SF, FA causes a significant rise in f_c and f_t. Overall, specimen 10S25R28D at 0.4 WC showed better results of f_c and f_t than other specimens of 10S because of the higher amount of R, curing age and low WC [77,78]. The trends of f_c and f_t results of 10S can be seen in Fig. 17.

The f_c and f_t values of MR 7S with respect to WC, R, curing age and quantity of SF and FA are presented in Fig. 18. The trend of the bars of f_c and f_t values is similar to that of the trend of 10S. The MR 7S showed better results than 10S due to higher amount of OPC, SF, and FA. 7S0R14D at 0.6 WC ratio showed fc of 11.24 MPa and ft value of 3.84 MPa that are the lowest values of f_c and f_t compared to the remaining specimens of 7S. 7S0R14D with 0.4 WC ratio gave a higher f_t value of 8.8 MPa while 7S25R28D with 0.WC ratio showed a higher f_c value of 18.21 MPa.

The MR 5.5S showed better mechanical properties than 10S and 7S. The improvement in f_c and f_t of 5.5S due to higher quantity of OPC, FA, and SF compared to the OPC, FA, SF amount used in 7S and 10S. 5.5S0R14D with WC 0.6 has low f_c and f_t of 13.82 MPa and 3.51 MPa, respectively. On the other hand, 5.5S25R28D at 0.4 WC showed higher f_c value of 21.05 MPa but 5.27 MPa value of f_t lower than f_t value of 6.53 MPa at 0.5WC. The behavior of f_c and f_t of 5.5S is presented in Fig. 19. In general, the variation of the dataset generated experimentally can be observed in Fig. 17, Fig. 18 and Fig. 19.

Table 4
Regression values of the trained ANN and ANFIS models.

IPAN Model	*R*-value
ANN-f_c	**0.997**
ANN-f_t	0.948
ANFIS-gbell-f_c	**0.978**
ANFIS-gbell-f_t	0.923
ANFIS-tri-f_c	0.921
ANFIS-tri-f_t	0.890
ANFIS-gauss-f_c	0.956
ANFIS-gauss-f_t	0.914

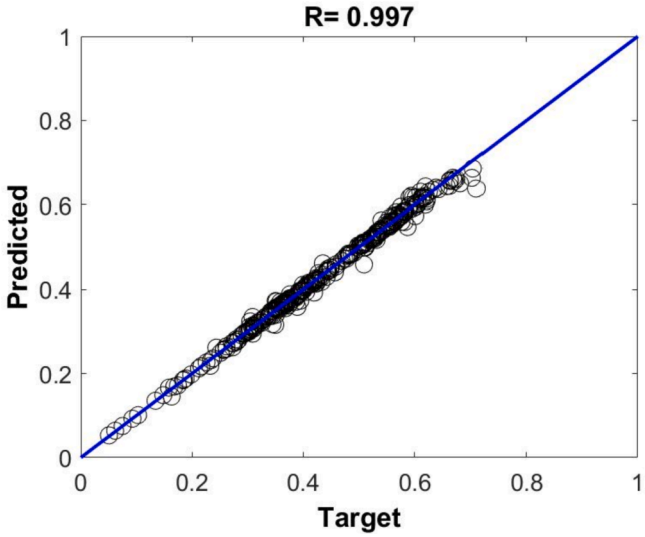

Fig. 15. Regression values of the optimized ANN model.

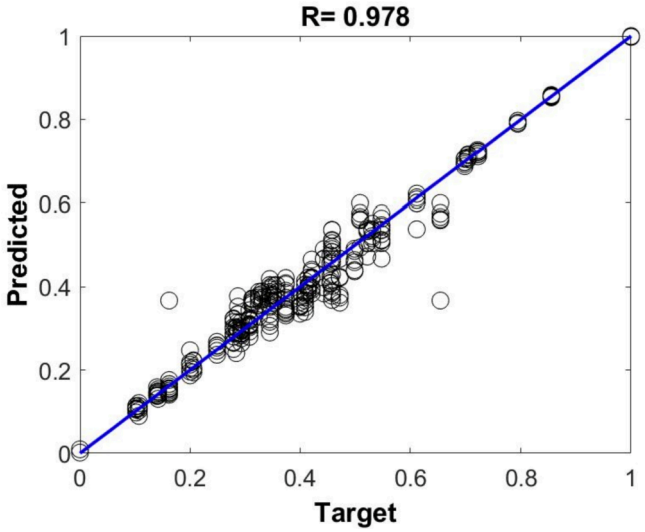

Fig. 16. Regression value of the optimized ANFIS model.

The compressive strength obtained from DT, such as the hydraulic press test, was compared with the one acquired through NDTs. The comparison of results showed that UPV and SH results also deviate from DT results. So, the NDT results popularly used, such as the ones based on UPV and SH, also contain some error and cannot be considered absolutely accurate.

The f_c values from conventional methods, such as HM, RH, UPV, for all specimens at 14 days and 28 days were compared. The results obtained from HM follow a pattern according to MR, WC ratio, amount of OPC, FA, and SF used, and curing age. On the other hand, the values of f_c calculated from RH and UPV do not follow the same pattern at few points. The irregular behavior presented by the values of f_c was probably due to error and inaccuracy of these techniques. The f_c values from HM are higher with 25% of SF, FA replacement, 28 days curing, and low WC ratio of 0.4 for all mix ratios. On the other hand, mix ratios with lower replacement, higher WC ratio, and 14 days of curing gave low f_c values. The f_c value calculated from RH for mix ratio 10S at 0.4 WC ratio at 14 days was higher at 15% of SF, and FA than the sample with 25% of SF, FA. Similarly, the f_c value calculated from UPV for 7S at 0.6 WC ratio and 14 days with 0% of SF and FA is higher than the f_c value for the 7S with 25% of SF and FA, 0.6 WC ratio, and 14 days of curing. The

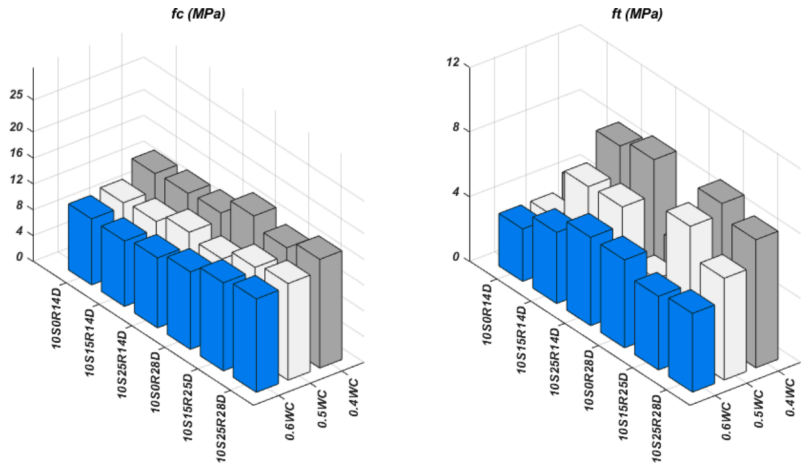

Fig. 17. Compressive and Tensile strength of mix ratios 1:3:6 at different W/C ratios.

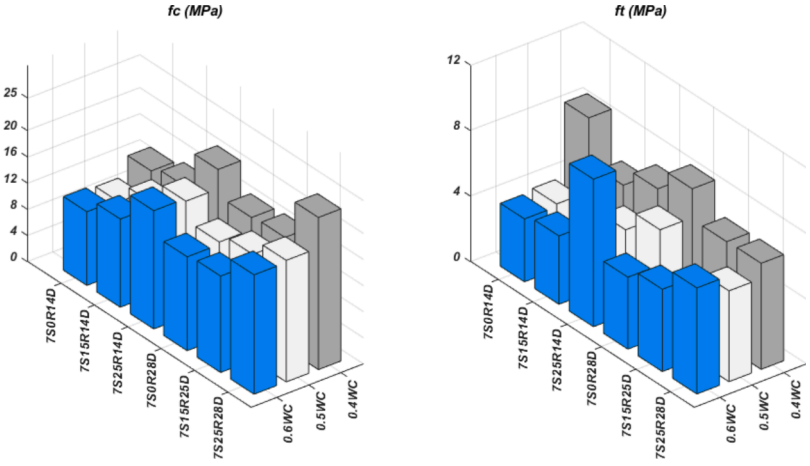

Fig. 18. Compressive and Tensile strength of mix ratios 1:2:4 at different W/C ratios.

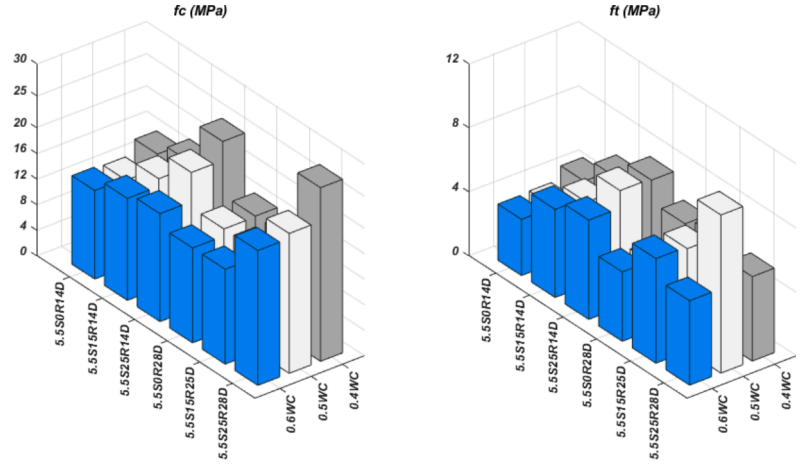

Fig. 19. Compressive and Tensile strength of mix ratios 1:1.5:3 at different W/C ratios.

comparisons of f_c values acquired from all methods and devices at 14 days and 28 days are presented in Fig. 20 and Fig. 21, respectively. The pattern in results of HM obtained values and irregularity in RH and UPV calculated values can be noticed.

6. Conclusions

In this work, we used Image processing, artificial neural network, and adaptive neuro-fuzzy inference system computational techniques for predicting the mechanical properties of hybrid concrete. The results obtained from destructive and non-destructive testing showed a high

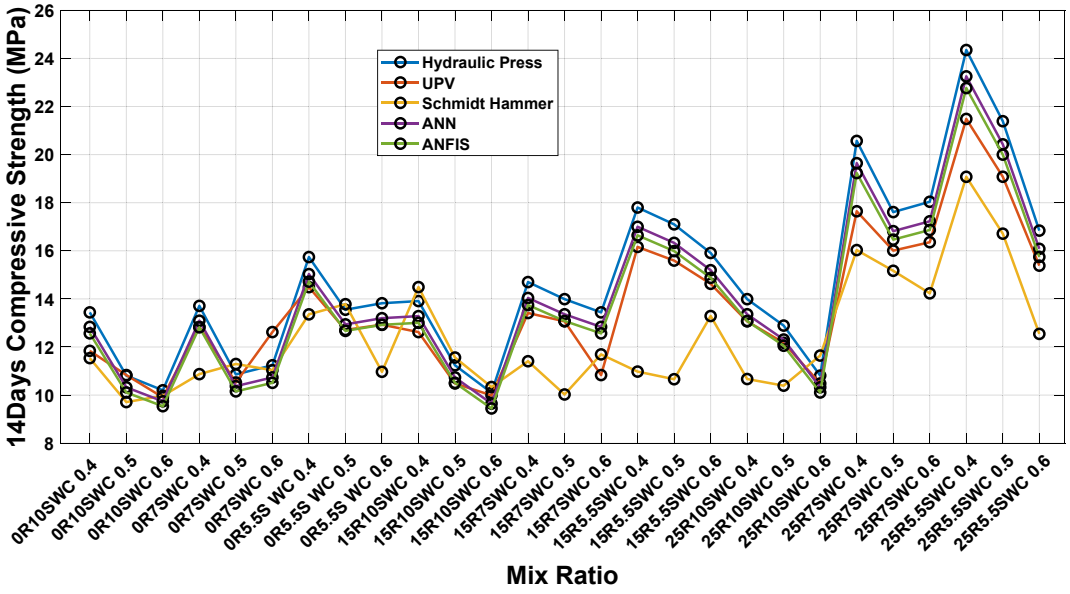

Fig. 20. Comparison of 14 days compressive strength of concrete obtained from IPAN, NDT and DT.

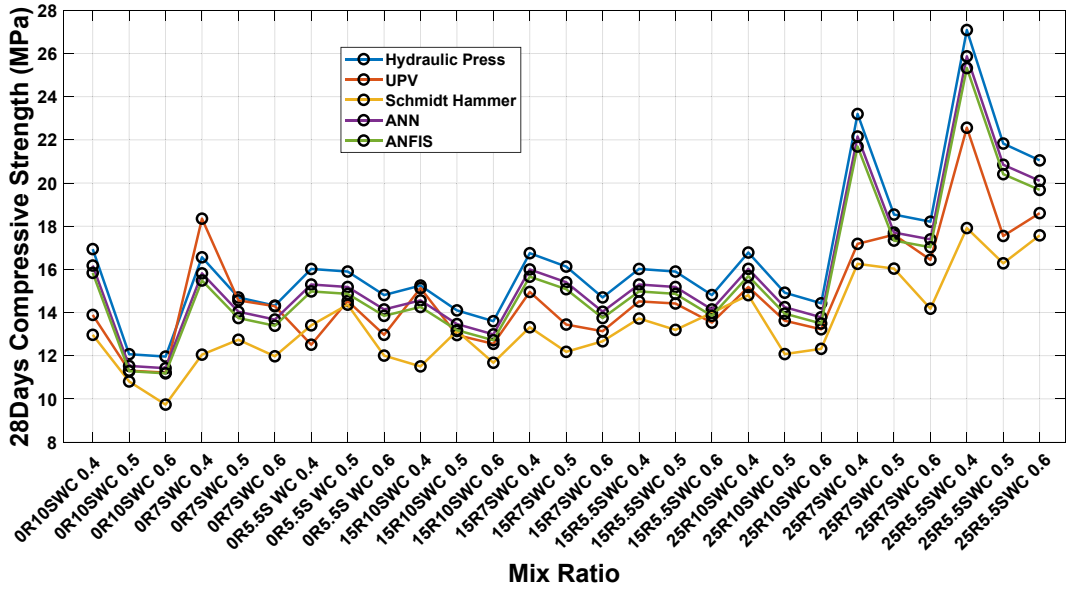

Fig. 21. Comparison of 28 days compressive strength of concrete obtained from IPAN, NDT and DT.

correlation with the mechanical features of concrete predicted using the proposed methodology. The proposed method (IPAN) is a combination of image processing and artificial neural network which utilizes statistical features extracted using image processing for training testing and validation of ANN and ANFIS. IPAN was trained using DT results and predicted results were calibrated with NDT results. IPAN-predicted results were compared with the DT results acquired from the laboratory tests as well as with NDT results of compressive strength obtained through UPV and SH. A comparison of the results showed that the proposed method can be utilized as an alternative NDT technique to predict the mechanical properties of concrete with high reliability and accuracy. The main conclusions of this research work are highlighted in the next paragraph.

The specimens of hybrid concrete which contained 25% cement replacement material (silica fume and fly ash) showed better strength compared to the specimens with 15% or 0% CRM. In a similar manner, the samples with 15% CRM showed better results than the ones with 0% CRM. This effect in strength was due to enhanced pozzolanic action because of the presence of silica fume and fly ash. Further, the compressive strength obtained from DT such as the hydraulic press test was compared with the one acquired through NDTs. The comparison of the results showed that UPV and SH results also deviate from DT results. So, the NDT results popularly used, such as the ones based on UPV and SH, also contain some error and cannot be considered 100% accurate. Values of the compressive and the tensile strength of concrete were related to the corresponding values estimated from the proposed methods, (IP, ANN) and (IP, ANFIS), together. The accuracy of the results largely depends on the data set. The accuracy obtained by IP/ANN (in terms of the *R* value) is 99.7% while the one obtained with IP/ANFIS is 97.8%.

CRediT authorship contribution statement

Muhammad Imran Waris: Software, Investigation, Formal analysis,

Writing – original draft. **Vagelis Plevris:** Conceptualization, Resources, Supervision, Validation, Formal analysis, Visualization, Writing – original draft, Writing – review & editing. **Junaid Mir:** Conceptualization, Validation, Software, Investigation, Formal analysis, Writing – original draft, Writing – review & editing. **Nida Chairman:** Software, Investigation, Writing – review & editing. **Afaq Ahmad:** Conceptualization, Validation, Software, Investigation, Formal analysis, Visualization, Writing – original draft, Writing – review & editing.

Declaration of Competing Interest

The authors declare that they have no known competing financial interests or personal relationships that could have appeared to influence the work reported in this paper.

Acknowledgements

The work is the research collaboration between the Department of Civil Engineering, University of Engineering and Technology, Taxila and the Department of Civil and Architectural Engineering, Qatar University. For the experimental work the funding was arranged under the research grant of PHEC/ARA/PIRCA/20529/22.

References

[1] A.M. Alani, A. Faramarzi, An evolutionary approach to modelling concrete degradation due to sulphuric acid attack, Appl. Soft Comput. 24 (2014) 985–993, https://doi.org/10.1016/j.asoc.2014.08.044.
[2] C.R. Farrar, K. Worden, An introduction to structural health monitoring, Philos. Trans. Royal Soc. A: Math., Phys. Eng. Sci. 365 (1851) (2007) 303–315, https://doi.org/10.1098/rsta.2006.1928.
[3] A. Ahmad, N.D. Lagaros, D.M. Cotsovos, Neural network-based prediction: the case of reinforced concrete members under simple and complex loading, Appl. Sci. 11 (11) (2021), https://doi.org/10.3390/app11114975.
[4] A. Ahmad, et al., Reliability analysis of strength models for short-concrete columns under concentric loading with FRP rebars through Artificial Neural Network, J. Build. Eng. 42 (2021), 102497, https://doi.org/10.1016/j.jobe.2021.102497.
[5] D.J. Armaghani, P.G. Asteris, A comparative study of ANN and ANFIS models for the prediction of cement-based mortar materials compressive strength, Neural Comput. Appl. (2020) 1–32, https://doi.org/10.1007/s00521-020-05244-4.
[6] B.F. Spencer, V. Hoskere, Y. Narazaki, Advances in computer vision-based civil infrastructure inspection and monitoring, Engineering 5 (2) (2019) 199–222, https://doi.org/10.1016/j.eng.2018.11.030.
[7] M. Georgioudakis, V. Plevris, A combined modal correlation criterion for structural damage identification with noisy modal data, Adv. Civil Eng. 2018 (2018) 3183067, https://doi.org/10.1155/2018/3183067.
[8] J.-H. Xu, et al., CO2 emissions reduction potential in China's cement industry compared to IEA's Cement Technology Roadmap up to 2050, Appl. Energy 130 (2014) 592–602.
[9] M. Dobiszewska, Waste materials used in making mortar and concrete, J. Mater. Educ. 39 (5–6) (2017) 133–156.
[10] R. Kurad, et al., Effect of incorporation of high volume of recycled concrete aggregates and fly ash on the strength and global warming potential of concrete, J. Cleaner Prod. 166 (2017) 485–502.
[11] R. Bajpai, et al., Environmental impact assessment of fly ash and silica fume based geopolymer concrete, J. Cleaner Prod. 254 (2020), 120147.
[12] J. Xiao, et al., Investigation on effect of aggregate on three non-destructive testing properties of concrete subjected to sulfuric acid attack, Constr. Build. Mater. 115 (2016) 486–495.
[13] C. Rocco, M. Elices, Effect of aggregate shape on the mechanical properties of a simple concrete, Eng. Fract. Mech. 76 (2) (2009) 286–298.
[14] R. Siddique, G. De Schutter, A. Noumowe, Effect of used-foundry sand on the mechanical properties of concrete, Constr. Build. Mater. 23 (2) (2009) 976–980.
[15] R. Siddique, Effect of fine aggregate replacement with Class F fly ash on the mechanical properties of concrete, Cem. Concr. Res. 33 (4) (2003) 539–547.
[16] Y. Huang, et al., Effects of coral, recycled and natural coarse aggregates on the mechanical properties of concrete, Constr. Build. Mater. 192 (2018) 330–347.
[17] M. Etxeberria, A. Gonzalez-Corominas, P. Pardo, Influence of seawater and blast furnace cement employment on recycled aggregate concretes' properties, Constr. Build. Mater. 115 (2016) 496–505.
[18] M. Lopez, L.F. Kahn, K.E. Kurtis, Characterization of elastic and time-dependent deformations in high performance lightweight concrete by image analysis, Cem. Concr. Res. 39 (7) (2009) 610–619, https://doi.org/10.1016/j.cemconres.2009.03.015.
[19] P.G. Asteris, et al., Investigation of the mechanical behaviour of metakaolin-based sandcrete mixtures, Eur. J. Environ. Civil Eng. (2017) 1–25, https://doi.org/10.1080/19648189.2016.1277373.
[20] A. Standard, Standard test method for compressive strength of cylindrical concrete specimens, ASTM C39 (2010).
[21] ASTM, A., ASTM C496/C496M-04e1 Standard Test Method for Splitting Tensile Strength of Cylindrical Concrete Specimens. Annual book of ASTM standards: section, 2008. **4**.
[22] Y. Javadi, V. Plevris, M.A. Najafabadi, Using LCR ultrasonic method to evaluate residual stress in dissimilar welded pipes, Int. J. Innovat., Manage. Technol. 4 (1) (2013) 170–174, https://doi.org/10.7763/IJIMT.2013.V4.384.
[23] J.A. Bogas, M.G. Gomes, A. Gomes, Compressive strength evaluation of structural lightweight concrete by non-destructive ultrasonic pulse velocity method, Ultrasonics 53 (5) (2013) 962–972, https://doi.org/10.1016/j.ultras.2012.12.012.
[24] D. Breysse, Nondestructive evaluation of concrete strength: an historical review and a new perspective by combining NDT methods, Constr. Build. Mater. 33 (2012) 139–163, https://doi.org/10.1016/j.conbuildmat.2011.12.103.
[25] R.M. Ferreira, S. Jalali, NDT measurements for the prediction of 28-day compressive strength, NDT E Int. 43 (2) (2010) 55–61, https://doi.org/10.1016/j.ndteint.2009.09.003.
[26] Z.-M. Sbartaï, et al., Combining NDT techniques for improved evaluation of concrete properties, Cem. Concr. Compos. 34 (6) (2012) 725–733, https://doi.org/10.1016/j.cemconcomp.2012.03.005.
[27] M. Shariati, et al., Assessment of longstanding effects of fly ash and silica fume on the compressive strength of concrete using extreme learning machine and artificial neural network, J. Adv. Eng. Comput. 5 (1) (2021) 50–74, https://doi.org/10.25073/jaec.202151.308.
[28] M. Shariati, et al., A novel hybrid extreme learning machine–grey wolf optimizer (ELM-GWO) model to predict compressive strength of concrete with partial replacements for cement, Eng. Comput. (2020) 1–23, https://doi.org/10.1007/s00366-020-01081-0.
[29] E.S. Chahnasir, et al., Application of support vector machine with firefly algorithm for investigation of the factors affecting the shear strength of angle shear connectors, Smart Struct. Syst. 22 (4) (2018) 413–424.
[30] M. Shariati, et al., Prediction of concrete strength in presence of furnace slag and fly ash using Hybrid ANN-GA (Artificial Neural Network-Genetic Algorithm), Smart Struct. Syst. 25 (2) (2020) 183–195.
[31] D. Li, et al., Application of polymer, silica-fume and crushed rubber in the production of Pervious concrete, Smart Struct. Syst. 23 (2) (2019) 207–214.
[32] S. Ganguly, A. Ahmed, F. Wang, Optimised building energy and indoor microclimatic predictions using knowledge-based system identification in a historical art gallery, eural Comput. Appl. (2019) 1–18.
[33] P.G. Asteris, V.G. Mokos, Concrete compressive strength using artificial neural networks, Neural Comput. Appl. 32 (15) (2020) 11807–11826, https://doi.org/10.1007/s00521-019-04663-2.
[34] V. Plevris, P.G. Asteris, Modeling of masonry failure surface under biaxial compressive stress using neural networks, Constr. Build. Mater. 55 (2014) 447–461, https://doi.org/10.1016/j.conbuildmat.2014.01.041.
[35] B. Vakhshouri, S. Nejadi, Prediction of compressive strength of self-compacting concrete by ANFIS models, Neurocomputing 280 (2018) 13–22, https://doi.org/10.1016/j.neucom.2017.09.099.
[36] H.-B. Ly, et al., Improvement of ANFIS model for prediction of compressive strength of manufactured sand concrete, Appl. Sci. 9 (18) (2019) 3841.
[37] A. Ahmad, D.M. Cotsovos, N.D. Lagaros, Framework for the development of artificial neural networks for predicting the load carrying capacity of RC members, SN Appl. Sci. 2 (4) (2020) 545, https://doi.org/10.1007/s42452-020-2353-8.
[38] M.Y. Mansour, et al., Predicting the shear strength of reinforced concrete beams using artificial neural networks, Eng. Struct. 26 (6) (2004) 781–799.
[39] C. Başyiğit, et al., Assessment of concrete compressive strength by image processing technique, Constr. Build. Mater. 37 (2012) 526–532, https://doi.org/10.1016/j.conbuildmat.2012.07.055.
[40] Özgen, C., *Evaluation of air void parameters of fly ash incorporated self consolidating concrete by image processing*. 2009, MIDDLE EAST TECHNICAL UNIVERSITY.
[41] E.K.K. Nambiar, K. Ramamurthy, Air-void characterisation of foam concrete, Cem. Concr. Res. 37 (2) (2007) 221–230, https://doi.org/10.1016/j.cemconres.2006.10.009.
[42] A.T.A. Dantas, M. Batista Leite, K. de Jesus Nagahama, Prediction of compressive strength of concrete containing construction and demolition waste using artificial neural networks, Constr. Build. Mater. 38 (2013) 717–722, https://doi.org/10.1016/j.conbuildmat.2012.09.026.
[43] D.K. Kim, et al., Application of probabilistic neural networks for prediction of concrete strength, J. Mater. Civ. Eng. 17 (3) (2005) 353–362.
[44] P.O. Awoyera, et al. Model development for strength properties of laterized concrete using artificial neural network principles. in Soft Computing for Problem Solving. 2020. Singapore: Springer Singapore.
[45] A.T. Amlashi, et al., Soft computing based formulations for slump, compressive strength, and elastic modulus of bentonite plastic concrete, J. Cleaner Prod. 230 (2019) 1197–1216, https://doi.org/10.1016/j.jclepro.2019.05.168.
[46] A. Ahmad, D.M. Cotsovos, N.D. Lagaros. *Assessing the reliability of RC code predictions through the use of artificial neural network*. in *1st International Conference on Structural Safety Under Fire & Blast. Glasgow, UK*. 2016.
[47] M.M. Alshihri, A.M. Azmy, M.S. El-Bisy, Neural networks for predicting compressive strength of structural light weight concrete, Constr. Build. Mater. 23 (6) (2009) 2214–2219, https://doi.org/10.1016/j.conbuildmat.2008.12.003.
[48] A.W. Oreta, K. Kawashima, Neural network modeling of confined compressive strength and strain of circular concrete columns, J. Struct. Eng. 129 (4) (2003) 554–561.
[49] G. Sakshi, Concrete mix design using artificial neural network, J. Today's Ideas - Tomorrow's Technol. 1 (1) (2013), https://doi.org/10.15415/jotitt.2013.11003.

[50] R. Gupta, M.A. Kewalramani, A. Goel, Prediction of concrete strength using neural-expert system, J. Mater. Civ. Eng. 18 (3) (2006) 462–466.
[51] I.C. Yeh, Modeling slump flow of concrete using second-order regressions and artificial neural networks, Cem. Concr. Compos. 29 (6) (2007) 474–480, https://doi.org/10.1016/j.cemconcomp.2007.02.001.
[52] A. Öztaş, et al., Predicting the compressive strength and slump of high strength concrete using neural network, Constr. Build. Mater. 20 (9) (2006) 769–775, https://doi.org/10.1016/j.conbuildmat.2005.01.054.
[53] I.-C. Yeh, Exploring concrete slump model using artificial neural networks, J. Comput. Civil Eng. 20 (3) (2006) 217–221, https://doi.org/10.1061/(ASCE)0887-3801(2006)20:3(217).
[54] C. Bilim, et al., Predicting the compressive strength of ground granulated blast furnace slag concrete using artificial neural network, Adv. Eng. Softw. 40 (5) (2009) 334–340, https://doi.org/10.1016/j.advengsoft.2008.05.005.
[55] B. Liu, T. Yang, Image analysis for detection of bugholes on concrete surface, Constr. Build. Mater. 137 (2017) 432–440, https://doi.org/10.1016/j.conbuildmat.2017.01.098.
[56] M. Mirrashid, H. Naderpour, Computational intelligence-based models for estimating the fundamental period of infilled reinforced concrete frames, J. Build. Eng. 46 (2022), 103456, https://doi.org/10.1016/j.jobe.2021.103456.
[57] M. Mirrashid, H. Naderpour, Recent trends in prediction of concrete elements behavior using soft computing (2010–2020), Arch. Comput. Methods Eng. 28 (4) (2021) 3307–3327, https://doi.org/10.1007/s11831-020-09500-7.
[58] H. Naderpour, M. Mirrashid, P. Parsa, Failure mode prediction of reinforced concrete columns using machine learning methods, Eng. Struct. 248 (2021), 113263.
[59] M. Mirrashid, H. Naderpour, Innovative computational intelligence-based model for vulnerability assessment of RC frames subject to seismic sequence, J. Struct. Eng. 147 (3) (2021) 04020350, https://doi.org/10.1061/(ASCE)ST.1943-541X.0002921.
[60] M. Mirrashid, H. Naderpour, Computational intelligence-based models for estimating the fundamental period of infilled reinforced concrete frames, J. Build. Eng. (2021), 103456.
[61] P.G. Asteris, V. Plevris, Anisotropic masonry failure criterion using artificial neural networks, Neural Comput. Appl. 28 (8) (2017) 2207–2229, https://doi.org/10.1007/s00521-016-2181-3.
[62] M.E.A. Ben Seghier, et al., On the modeling of the annual corrosion rate in main cables of suspension bridges using combined soft computing model and a novel nature-inspired algorithm, Neural Comput. Appl. 33 (23) (2021) 15969–15985, https://doi.org/10.1007/s00521-021-06199-w.
[63] N. Aalimahmoody, et al., BAT algorithm-based ANN to predict the compressive strength of concrete—A comparative study, Infrastructures 6 (6) (2021), https://doi.org/10.3390/infrastructures6060080.
[64] H. Naderpour, M. Mirrashid, Bio-inspired predictive models for shear strength of reinforced concrete beams having steel stirrups, Soft. Comput. 24 (16) (2020) 12587–12597, https://doi.org/10.1007/s00500-020-04698-x.
[65] S. Arasan, et al., Correlation between shape of aggregate and mechanical properties of asphalt concrete: digital image processing approach, Road Mater. Pavement Design 12 (2) (2011) 239–262.
[66] S. Van der Walt, et al., scikit-image: image processing in Python, PeerJ 2 (2014), e453.
[67] Y.-F. Liu, et al., Concrete crack assessment using digital image processing and 3D scene reconstruction, J. Comput. Civil Eng. 30 (1) (2016) 04014124.
[68] G. Dogan, M.H. Arslan, M. Ceylan, Concrete compressive strength detection using image processing based new test method, Measurement 109 (2017) 137–148.
[69] O. Akkoyun. An evaluation of image processing methods applied to marble quality classification. in 2010 2nd International Conference on Computer Technology and Development. 2010. IEEE.
[70] V. Plevris, Innovative computational techniques for the optimum structural design considering uncertainties. 2009, National Technical University of Athens: Athens, Greece. p. 312.
[71] A. Keshavarzi, et al., Application of ANFIS-based subtractive clustering algorithm in soil Cation Exchange Capacity estimation using soil and remotely sensed data, Measurement 95 (2017) 173–180, https://doi.org/10.1016/j.measurement.2016.10.010.
[72] A. Sadrmomtazi, J. Sobhani, M.A. Mirgozar, Modeling compressive strength of EPS lightweight concrete using regression, neural network and ANFIS, Constr. Build. Mater. 42 (2013) 205–216, https://doi.org/10.1016/j.conbuildmat.2013.01.016.
[73] D.G. Daniel, C.L. Lobo, *User's Guide to ASTM Specification C 94 on Ready-mixed Concrete*. 2005: ASTM International, ISBN: 0803133634.
[74] Committee, A., I.O.f. Standardization. *Building code requirements for structural concrete (ACI 318-08) and commentary*. 2008. American Concrete Institute.
[75] ASTM, C., *Standard practice for making and curing concrete test specimens in the field*. 2012.
[76] M. Özen, İ. Yaman, M. Güler, Identifying an optimal shape parameter to estimate grain size distribution of concrete samples using imaging techniques. Advanced in Civil Engineering Conference'12, 2012.
[77] D. Ravina, P. Mehta, Compressive strength of low cement/high fly ash concrete, Cem. Concr. Res. 18 (4) (1988) 571–583.
[78] H.A. Toutanji, T. El-Korchi, The influence of silica fume on the compressive strength of cement paste and mortar, Cem. Concr. Res. 25 (7) (1995) 1591–1602.
[79] W. Wu, et al., The effect of fly ash and silica fume on mechanical properties and durability of coral aggregate concrete, Constr. Build. Mater. 185 (2018) 69–78.
[80] C805/C805M, A. *Standard test method for rebound number of hardened concrete*. 2013. American Society for Testing and Materials West Conshohocken, USA.
[81] Astm, C., *597, Standard test method for pulse velocity through concrete*. ASTM International, West Conshohocken, PA, 2009.
[82] U. Petronas, *Mean and standard deviation features of color Histogramusing Laplacian filter for content-based image retrieval*. J. Theor. Appl. Inf. Technol., 2011. **34**(1).
[83] S. Sergyan. Color histogram features based image classification in content-based image retrieval systems. in 2008 6th International Symposium on Applied Machine Intelligence and Informatics. 2008. IEEE.
[84] G. Dogan, M.H. Arslan, M. Ceylan, Statistical feature extraction based on an ANN approach for estimating the compressive strength of concrete, Neural Network World 25 (3) (2015) 301.
[85] H. Arslan, M. Ceylan, Judging primary school classroom spaces via artificial neural networks model. Gazi Univ. J. Sci., 2012. **25**(1): p. 245-256.
[86] A. Ahmad, V. Plevris, Q.-u.-Z. Khan, Prediction of properties of FRP-confined concrete cylinders based on artificial neural networks, Crystals 10 (9) (2020), https://doi.org/10.3390/cryst10090811.
[87] M.H. Arslan, An evaluation of effective design parameters on earthquake performance of RC buildings using neural networks, Eng. Struct. 32 (7) (2010) 1888–1898, https://doi.org/10.1016/j.engstruct.2010.03.010.
[88] M.H. Arslan, et al., Prediction of force reduction factor (R) of prefabricated industrial buildings using neural networks, Struct. Eng. Mech. 27 (2) (2007) 117–134.
[89] M.T. Hagan, M.B. Menhaj, Training feedforward networks with the Marquardt algorithm, IEEE Trans. Neural Networks 5 (6) (1994) 989–993.
[90] A.R. Ghumman, et al., Simulation of pan-evaporation using penman and hamon equations and artificial intelligence techniques, Water 13 (6) (2021), https://doi.org/10.3390/w13060793.
[91] M. Babanezhad, et al., Artificial intelligence simulation of suspended sediment load with different membership functions of ANFIS, Neural Comput. Appl. 33 (12) (2021) 6819–6833.
[92] M. Jalal, et al., Strength and dynamic elasticity modulus of rubberized concrete designed with ANFIS modeling and ultrasonic technique, Constr. Build. Mater. 240 (2020), 117920.